RESEARCH

Visible Emission Line Spectroscopy of the Solar Corona During the 2019 Total Solar Eclipse

Gabriel D. Muro[1,2] ⓘ · Matt Gunn[1] ⓘ · Stephen Fearn[1] · Tomos Fearn[1] ⓘ · Huw Morgan[1] ⓘ

Abstract

Spectroscopic measurements of the low solar corona are crucial to understanding the mechanisms that heat the corona and accelerate the solar wind, yet the lowest solar radii ($R_\odot$) of the corona are difficult to observe. Our expedition collected narrow wavelengths of visible light at 530.3, 637.4, and 789.2 nm emitted by Fe XIV, X, and XI ions, respectively, from the total solar eclipse on 2019 July 2 at 20:40 UTC in Rodeo, Argentina with a bespoke 3-channel spectrometer. This paper describes the instrument and data calibration method that enables diagnostics out to $\approx 1.0 \ R_\odot$ above the solar limb within a bright helmet streamer. We find that Fe X and XI lines are dominant through 0.3 $R_\odot$, with Fe XIV maintaining a stronger signal at higher elevations. Thermal line width broadening is consistent with 1.5 MK for the cooler Fe X, 2 MK for Fe XI, and 3 MK for the hotter Fe XIV line, which can be interpreted as differing density scale heights within isolated, isothermal flux tubes. The Doppler measurements correspond to bulk plasma motion ranging from -12 to $+2.5$ km s^{-1}, with Fe XIV moving at nearly an assumed solid body rotation rate throughout 1.0 $R_\odot$. After considering coronal rotation, these measurements are likely associated with plasma motion along the dominant longitudinal orientation of the magnetic field at the streamer base within 0.4 $R_\odot$. These results show that high-resolution spectroscopy of visible light offers valuable diagnostics of the low corona, and lend insight into the interconnected loop complexity within helmet streamers.

Keywords Eclipse · Visible light spectroscopy · Dynamics · Magnetic fields · Corona

1. Introduction

The solar corona is an environment of hot, magnetized plasma that provides a varying contribution to the solar wind as it is accelerated by the Sun's magnetic field and flows away into interplanetary space. Many aspects of this environment are poorly understood despite advancements in observations and models, including the source regions, acceleration, and

✉ G.D. Muro
  gabemuro@gmail.com

1   Department of Physics, Aberystwyth University, Ceredigion, Cymru, SY23 3BZ, UK

2   California Institute of Technology, Pasadena, CA, 91125, USA

nature of the slow solar wind (e.g. Cranmer, Gibson, and Riley, 2017), the structure and dynamics of the high-density streamer belts (e.g. Tsurutani et al., 2006; Morgan and Habbal, 2010; Morgan and Cook, 2020), the formation and evolution of small-scale variations in the slow solar wind (e.g. McComas et al., 2019; Alzate et al., 2021; Morgan, 2021), the mechanisms for heating and acceleration of the plasma (e.g. Parker, 1988; Van Doorsselaere et al., 2020), and the distance range at which this energy deposition occurs (e.g. Tu et al., 2005). These knowledge gaps arise from both the technical difficulties of remote-observing the Thomson scattered light from electrons and ion line emission, and interpreting the integrated emission along an extended line-of-sight (LOS) in the optically-thin medium.

The very low corona, heliocentric distance 1 to ≈ 1.3 solar radii ($R_\odot$), has been routinely observed by extreme ultraviolet (EUV) imagers in multiple bandpasses hosted by a succession of spacecraft. EUV spectral observations can be made off-limb to limited distances (Culhane et al., 2007; SPICE Consortium et al., 2020). There is excellent coverage of the broadband visible corona at distances over 2 $R_\odot$ by space-based coronagraphs over the past two solar cycles, although space- and ground-based coronagraphs observing closer to the Sun suffer from stray light and other difficulties. The UltraViolet Coronagraph Spectrometer (UVCS, Kohl et al., 1995) onboard the Solar and Heliospheric Observatory (SOHO, Domingo, Fleck, and Poland, 1995) observed ultraviolet spectra of hydrogen, oxygen, and other ions at distances from just above 1 to 6 $R_\odot$ or greater, leading to several key discoveries of the corona and solar wind acceleration (e.g. Habbal et al., 1997; Li et al., 1998; Suleiman et al., 1999; Cranmer et al., 1999; Antonucci, 2000; Morgan, Habbal, and Li, 2004; Kohl et al., 2006), although the presence of large sunspots could lead to considerable uncertainties in certain diagnostics (Morgan and Habbal, 2005).

The short period of totality during some solar eclipses, where the bright photospheric light is entirely blocked, provides a valuable opportunity to observe the corona in great detail, from distances very close to the Sun out to several solar radii. As well as offering an opportunity to develop subsequent generations of ground- or space-based coronagraphic instruments (imagers and spectrometers), the observations have led to a legacy of discoveries.

Early discovery of thousands of spectral lines were identified in the chromospheric flash spectrum of total solar eclipses in the 1930's by Menzel (1930), many of which were unknown in origin until Edlen extrapolated ionization sequences of heavy elements like iron, nickel, calcium, etc. (Edlén, 1941). These chromospheric emission lines contrasted with the spectrum of the K-corona, created by photospheric Thomson scattered light off of free electrons, where high electron velocities blur absorption lines so that its spectrum appears as a smooth continuum (Menzel and Pasachoff, 1968). E-corona emission lines of Fe XIV at 530.3 nm & Fe X at 637.4 nm have long been regularly isolated during total solar eclipses, with the use of techniques such as Fabry-Perot interferometers in the 1950's, and the interpreted kinetic temperatures well over 10^6 K within the first solar radius above the solar disk (Jarrett and von Klüber, 1955, 1961). Corresponding ultraviolet transition lines were then discovered with sounding rockets in the 1970's during total solar eclipses, as slitless spectrographs were able to identify Lyman-α hydrogen lines as well as dozens of other ion emission lines within the corona (Gabriel et al., 1971). A significant amount of progress occurred in the 1973 total solar eclipse as a Concorde airplane followed the totality path for 74 minutes with a suite of instruments that mapped spectra in ultraviolet, visible, and infrared wavelengths (Beckman et al., 1973). It was concluded that the F-corona's thermal emission was largely due to reflection of photospheric light off of dust out to several solar radii, but did not act as a perfect mirror in infrared as it did visible light, making distinguishing the K-corona from the F-corona possible. Léna et al. (1974) studied Doppler shift contributions to line width with multi-slit spectral observations during the 1980 total solar eclipse, and line

widths and Doppler broadening were estimated to correspond to temperatures of 4.6×10^6 K and turbulent velocities of 30 km s^{-1}, respectively (Singh, Bappu, and Saxena, 1982). Coordinated efforts to observe soft X-rays, in addition to other wavelengths via spectropolarimetry, during the 1988 eclipse allowed for coronal density and temperature structures to be determined from ratios of Fe ions in many wavelengths (Guhathakurta et al., 1992; Habbal, Esser, and Arndt, 1993). Arrays of white light and narrowband imagers combined with short-cadence arrays of cameras led to the discovery of complex, fine-scale, highly dynamic structures within the first solar radius above the limb during the 1991 total solar eclipse (Koutchmy et al., 1994). Soon after, in 1994, the shape of weak depressions at 390 and 430 nm in the coronal spectrum was compared with a theoretical electron-scattered spectrum to determine the electron thermal motion directly (Ichimoto et al., 1996). Polarized brightness measurements from the 1996 total solar eclipse were analyzed via an inversion method that determined the electron density within the low corona (Quémerais and Lamy, 2002). During the 2001 total solar eclipse, spectral data from several wavelengths were modelled to estimate the bulk flow speed of the solar wind within the low corona (Reginald et al., 2003).

The most prolific set of eclipse observations and discoveries during the 21st century have been made by an international group of collaborators led by Prof. Shadia Habbal, of the University of Hawaii. During the 2006 total solar eclipse, high-resolution broadband white-light images, subject to advanced image processing (Druckmüller, Rušin, and Minarovjech, 2006), combined with narrowband imaging in several visible or near-infrared emission lines, led to understanding that the Fe XI emission line at 789.2 nm line has a significant radiative component during its excitation process, which enables observations to large distances in the corona (Habbal et al., 2007b,a). The narrowband imagers have concentrated on coronal forbidden lines, most notably the three brightest visible lines of iron emission: Fe X, Fe XI, Fe XIV, which represent equilibrium temperatures of 0.9, 1.3, 1.9 MK, respectively. With data from the 2006 and 2008 total solar eclipses, the electron temperature from intensity ratios of emission lines was determined for regions where the plasma was collisional, as well as determining the radial distance where collisions ceased (Habbal et al., 2009). These Fe ions provide diagnostic capabilities for exploring the inner corona, such as in the 2010 eclipse, when the long-standing ambiguity of temperature and magnetic structure of prominence cavities was resolved (Habbal et al., 2010). A decade's worth of high-resolution white light total solar eclipse observations were subjected to advanced image processing to find the link between prominences and large-scale coronal structures, including the source of the slow solar wind (Habbal, Morgan, and Druckmüller, 2014). Atypical structures within the corona were then explored in the 2012 and 2013 eclipses with white light imaging, and space-based EUV images were found to be the result of long-lasting remnants of faint coronal mass ejections (CMEs; Alzate et al., 2017). More recently, the arsenal of instrumentation has been expanded to include an innovative spectrometer offering high-resolution spectra of Fe XI, and Fe XIV. Observations by this instrument during the total solar eclipse of 2015 led to the discovery of prominence material embedded within a CME front (Ding and Habbal, 2017). Also at the 2015 eclipse, Fe XI and XIV filtered images led to measuring the distance where fixed ionization states for Fe ions within the solar wind occurred before further expanding into interplanetary space Boe et al. (2018). During the 2019 eclipse described in this study, an airborne spectrometer was concurrently flown at high-altitude to obtain measurements of Fe IX, Si X and the first observation of S XI (Samra et al., 2022; Del Zanna et al., 2023) which expanded the list of coronal near-infrared lines.

Funded by the United Kingdom's Science, Technology, and Facilities Council (STFC, see Acknowledgments), and in collaboration with Prof. Adalbert Ding, a prototype 2-channel spectrometer was built at Aberystwyth and tested during the total solar eclipse of 2015.

Based on our experience in that eclipse, a more compact and robust design was developed and built at Aberystwyth for use in following eclipses. This low-cost, 3-channel spectrometer, collects spectra of the three main Fe ion lines in the visible and near infrared range along a spatially linear slit at a very high order, enabling fine spectral resolution. During an eclipse, the spectrometer can be sat at rest whilst the Sun pans across the sky, thus scanning a large region of the corona during the minutes of totality.

This study gives a description of the spectrometer, observations, and presents results arising from the July 2019 total solar eclipse in Argentina. Section 2 describes the overall instrument design, calibration methods, and optical corrections carried out on the data. Section 3 describes the collection of data during totality, analysis of emission spectra to determine spectral diagnostics. Section 4 shows the 2D mapping of coronal spectra along with analysis results and interpretation of selected sets of data. Section 5 discusses the spectral results within the white light coronal context of a helmet streamer and provides a brief summary.

2. Instrument Design and Calibration Methods

This section summarises the design and concept of the 3-channel spectrometer, and the methods for calibrating the data.

2.1. The 3-Channel Spectrometer Design

The instrument is a 3-channel push-broom spectrometer with a white-light entrance camera. The spectral range of the channels is approximately centered on three iron emission lines: Fe XIV, Fe X, and Fe XI which correspond to 530.3 nm, 637.4 nm, and 789.2 nm, respectively. Figure 1 shows a schematic diagram of the device. Incoming light passes through a Canon 300 mm f/2.8 SLR lens and focused onto an etched chrome-on-glass entrance slit-mirror angled at 30° toward a secondary mirror that redirects light into a 25 mm lens then toward a monochrome Atik GP camera, known hereafter as the "context camera." The context camera covers a $\approx 36' \times 47'$ region of sky, which is slightly larger than the solar disk.

The light beam that passes through the mirror entrance slit is collimated by a 100 mm f/2.8 mount machine vision lens and then directed to the dichroic beam splitter (DBS) of the first spectrometer channel. The DBS is coated onto a Schott long-pass filter, and reflects green light toward an Echelle diffraction grating. The grating disperses the incident light at a high order (see Table 1) for measurement by a monochrome Atik Infinity CCD camera fitted with a 50 mm C mount machine vision lens and order-sorting bandpass filter.

Longer wavelength light is transmitted by the DBS of the first channel onto the DBS of the second channel, which reflects red light onto the grating of the second channel, and transmits longer wavelengths (see Table 1 and Figure 2). The second and third channels have similar optical components to the first, except a mirror is used instead of a DBS for the third channel. Details including the diffraction grating orientation, theoretical resolution, and spectral range of each channel are listed in Table 1. The response of each channel's DBS is shown in Figure 2.

All optical and CCD elements are mounted on an aluminum plate and sealed with a carbon fibre lid to suppress stray light. The entire device is approximately 15 kg and fits within a standard backpack. An image of the open optics case is shown in Figure 3. An electric thermocouple is placed within the case to monitor internal temperature, and other electronic elements are sealed on the underside of the aluminum plate to minimise thermal or other interference.
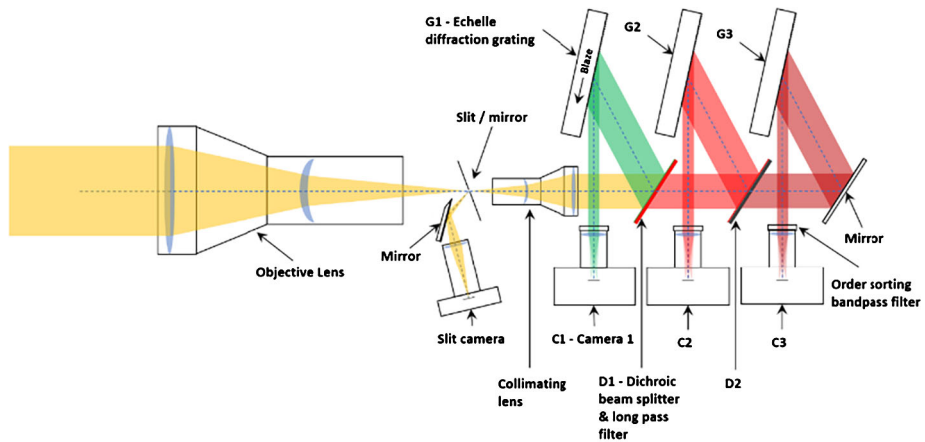
Figure 1 A schematic diagram of the spectrometer's optical path. Incoming light (yellow) is focused through the objective lens onto a mirror which has a vertical (pointing out of the diagram) narrow entrance slit. The mirror reflects light toward the slit camera to provide white light context of the dark line entrance slit. Light passing through the slit goes through a collimating lens before encountering the first dichroic beam splitter that reflects green light (≈ 550 nm and shorter) toward the echelle diffraction grating, whilst transmitting longer wavelengths. The reflected green light is dispersed by the echelle grating, and filtered by an order-sorting bandpass filter. A camera records the spectra, with the x-axis of the detector aligned in the spectral direction, and the y-axis aligned with the spatial direction of the vertical slit. The light that is transmitted by the dichroic splitter passes to the dichroic splitter of the second channel, which reflects red light (≈ 700 nm and shorter). The mirror of the third channel reflects the remaining light.

Table 1 Specifications of the 3-channel spectrometer.

Channel target wavelength (nm)	530.3	637.4	789.2
Bandpass filter: centralized wavelength $\times$ FWHM (nm)	527×20	650×40	775×46
Grating Periodicity (lines/mm)	79	79	52.67
Grating blaze angle	$63.43°$	$62°$	$63.5°$
Diffraction order	42	34	42
Incident angle α	$53.06°$	$47.82°$	$50.76°$
Diffraction angle β	$73.8°$	$76.18°$	$76.24°$
Free Spectral Range (nm)	12.6	18.7	18.8
Detected Spectral Range (nm)	15.01	15.96	19.31
Diffraction limit (nm)	0.001	0.0014	0.0017
Sampling resolution (nm/pixel)	0.011	0.011	0.014

2.2. Flatfields and Darkfields

Flatfield measurements were taken using a Labsphere $12''$ uniform light source integrating sphere system. The interior of the enclosed sphere is coated with white diffuse reflective paint to produce an even white background illuminated by incandescent light sources. The integrating sphere was powered to 10 μA while taking spectra, so that a good signal strength or digital number (DN) was received at all pixels without saturation.

The flatfield images of Figure 4a, 4b, and 4c show that the combination of CCD sensitivity at different wavelengths, dichroic mirror semi-reflectivity, and high order of the Echelle grating creates a highly non-uniform, yet reasonably smooth response for the spectral chan-
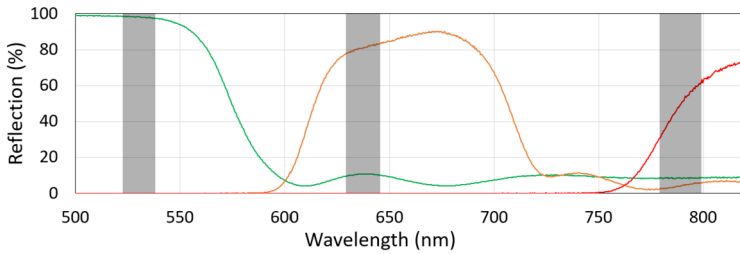
Figure 2 Dichroic beam splitter reflection for each wavelength. The green, orange, and red lines are light reflected by the DBS for the first, second, and third channels, respectively, targeting the iron emission lines at 530.3, 637.4, and 789.2 nm. The shaded grey areas represent the detected spectral range measured in each spectrometer channel.
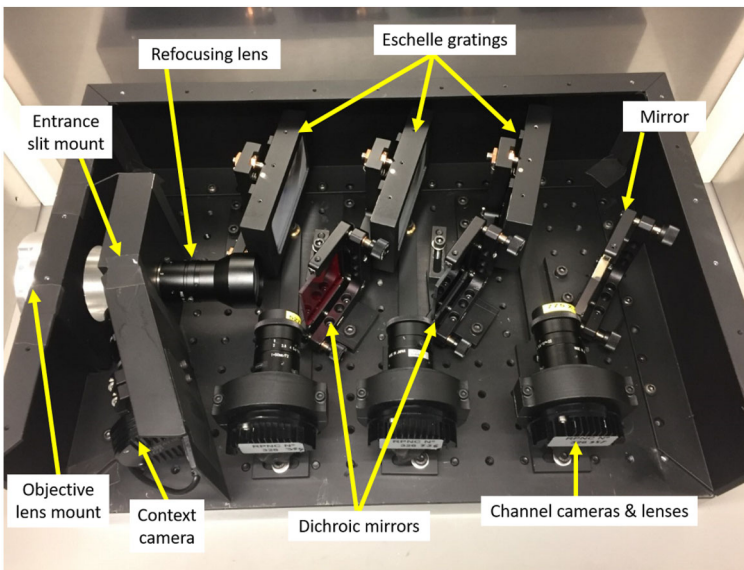

Figure 3 Image of the opened spectrometer assembly, with the alignment corresponding to the schematic diagram of Figure 1.

nels. The slope of the plotted lines in Figure 4d, 4e, and 4f across the entire 1392 pixels of each image is a negligible concern since the target Fe ion spectral signatures are only ≈ 25 pixels wide and located on flatter areas of the graphs.

Darkfield images are sets of spectral images made with a cover over the objective lens with equal exposure time as the flatfield images. For example, the 530.3 nm channel with 1 second exposures, darkfield and flatfield images resulted in DN counts of ≈ 850 to ≈ 4200, respectively, across the region of interest within the spectra. Flatfield and darkfield images were processed for each channel by averaging individual pixels over a sets of these images, and then dividing each pixel by the mean of their respective images to find the typical response for each channel.

In each channel, the processed darkfield is then subtracted from both the processed flatfield and eclipse observation images. Finally, the eclipse observation images are divided by
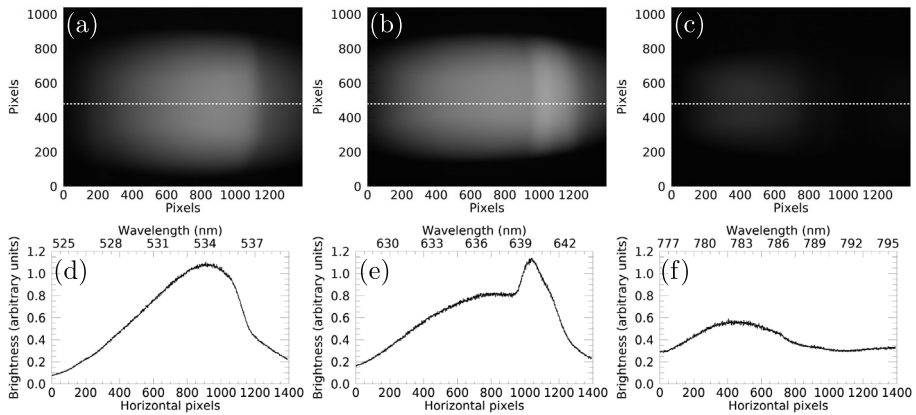
Figure 4 Top row: Examples of the (a) Fe XIV, (b) Fe X, and (c) Fe XI channel flatfield images taken with an integrating sphere. The x-axis is the spectral dimension in pixels, and the y-axis is the spatial dimension (along the spectrometer entrance slit) in pixels. A horizontal dashed line is approximately centered on where the intensity is measured. Bottom row: Normalized flatfield intensity of (d) Fe XIV, (e) Fe X, and (f) Fe XI in arbitrary units measured along the horizontal dashed lines. The wavelength range is shown in nanometers, as well as pixels measured horizontally across the images above.

the flatfield to create a corrected eclipse image, with the DN contribution from instrumental effects reduced by roughly 1.0 to 1.3 from resulting intensity graphs.

2.3. Cross-Calibration of Spectrometer Channels

Cross-calibration of the spectrometer channels is achieved through the relative intensities of the integrating sphere images and a broadband light intensity meter within the integrating sphere. There are many reasons why spectral channels have a varying response to input light, including the transmission and reflectance of the two DBS, the camera wavelength response, and the wavelength response of other optical components, including the order-sorting bandpass filters.

Within the integrating sphere, an incandescent bulb is set to a current of 10 μA to create a smooth spectral profile which is measured at 1 nm increments by the light intensity meter. These profiles give the input light flux, I_λ, at $\lambda = 530, 637,$ and 789 nm in units of $\mathrm{W\,m^{-2}\,sr^{-1}}$. Next, we isolate regions of the spectrometer images centered on the expected position of the eclipse spectral line (this is to avoid the large DN variation near the image edges) to calculate a mean DN value. This value is divided by the exposure time to give a count rate, which we label as M_λ, measured in $\mathrm{DNs^{-1}}$, for each channel.

Since the ratio between coronal spectral lines during the eclipse was unknown, due to lack of broadband spectra, we used the known light source ratios of I_λ at the same spectral positions to get the cross-calibration factor f_λ:

$$f_\lambda = \frac{M_\lambda I_\lambda}{I_{789}}. \tag{1}$$

We use the 789.2 nm, Fe XI, near-infrared channel as a master channel against which the other two channels are cross-calibrated to alter their DN by the appropriate f_λ. While this is not a direct analog for the corona during totality, it does ensure that light transmission is correct relative to the optics of each spectral channel.

Figure 5 Measured light intensity produced by incandescent bulbs within the integrating sphere for wavelength ranges of interest (black lines), mean uncalibrated intensity across a region of interest of each channel's detector (red squares), and intensities following cross-calibration (blue diamonds).
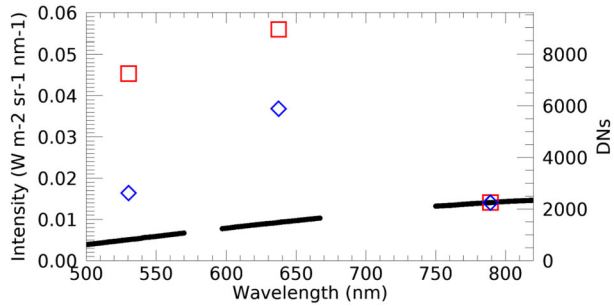
By applying Equation 1, the resulting cross-calibration is shown in Figure 5, which displays the wavelength-dependent measurements. As is expected, as the first spectral channel in the optical assembly, the 530 nm channel is reduced by roughly two-thirds. The second channel in the optical assembly, 637 nm, is reduced by roughly one-third. The last channel in the optical assembly, 789 nm, is left unchanged since it is used by our cross-calibration method as the reference.

2.4. Straightening the Optical 'Smile' Artifact

Optical artifacts are inherent to spectrometers with a linear slit and produce a curved 'smile' distortion, as shown in the uncorrected spectral image of Figure 6. This occurs due to aberrations in the spectrometer optics and leads to the misregistration of pixels across the field of view in the spectral dimension (e.g. Yuan et al., 2019). We developed a semi-automated trigonometric approach for correcting the optical smile.

Figure 6a shows how the automated detection of the curves in each channel was found via local minima of faint absorption lines from a laboratory light source with a set of clear absorption lines. A lab source was chosen in lieu of coronal spectra due to the spread of lines across the full image; the spatial location of spectral lines in the image was unimportant since the distortion is applied across the entire image. The local minimum (?) of the spectral line center across the slit were identified, and the position of each minimum pixel on the detector was recorded. The result of this detection is a set of pixels, which outlines an incomplete circle, as shown by the red points in Figure 6a. A fitting routine takes the set of points and finds the center location and radius of the circle that best fits the points, as shown in green in Figure 6a. The center point is located beyond the boundary of the actual image. Once the circle parameters are found for each channel, it is possible to correct for the optical smile.

The location of the spectral line of interest in Figure 6a, approximately 2/3rds from the left side of the image, is used for shifting pixels in the correction process. Essentially, every pixel in the image is compared against the radius between the circle center and the spectral line of interest located directly horizontal to it. For that same horizontal set of pixels, no shifting is required. Above and below the horizontal set of pixels, the difference between the edge of the circle and the vertical dashed line determines the pixel shift needed to straighten the 'smile'. The end result is a corrected image where the Fe ion spectral line of interest is vertical, as shown in Figure 6b.

Note that this correction is only strictly valid for the position of the spectral line of interest in each channel. As can be seen in Figure 6b, the correction becomes increasingly invalid for pixels at a spectral position far from the line of interest. Further correction was not attempted to avoid overcorrection of the tenuous coronal data and a lack of resources in quantifying them. Furthermore, we analyze only the spectral line of interest in this dataset, and any further warping corrections towards the spectral range limits is redundant.
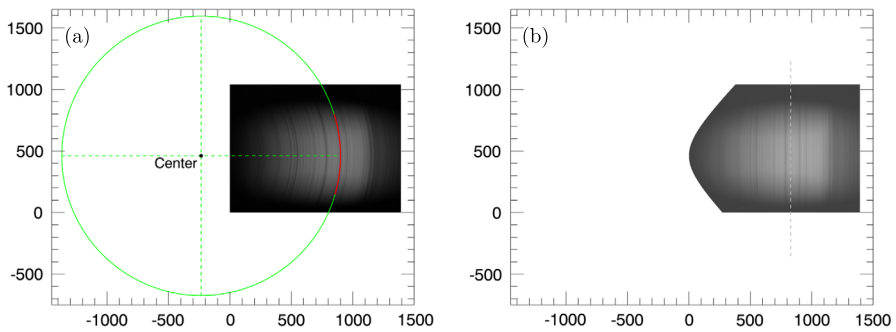
Figure 6 (a) An uncorrected spectral image, with red points tracing the local minima of a strong absorption line. The green circle shows the circle that best fits these points. From the fitting, the circle center is at $x, y = -234, 461$ pixels, as indicated by the vertical and horizontal dashed green lines. Note that this center is beyond the leftmost boundary of the image. (b) Corrected image with pixels shifted to correspond to the wavelength of interest, denoted by a dashed line.

2.5. Wavelength Calibration

Based on careful identification of known spectral lines from laboratory sources, we estimated the spectral pixel-width resolution of the spectral image data. The results range from 0.011 to 0.014 nm per pixel for the different channels (detailed in Table 1). Both neon and krypton gas calibration lamps were used for this purpose, with comparisons of measured spectra made against the National Institute of Standards & Technology database for strong lines of neutral elemental gas emissions, which allowed for reliable wavelength identification (Kaufman, 1993; Saloman and Sansonetti, 2004). To avoid complication with the 'smile' straightening correction, these calibrations were performed at the same vertical baseline location within the spectral images as the fitted circle adjustments, or in other words, at the horizontal slice of the detector corresponding to the vertical position of the circle center, as shown in Figure 6a. The calibration lamp measurements were made in a dark optics laboratory, and the pixel location and intensity of the emission line peaks recorded.

Figure 7 shows selected spectra of Fe ions measured during the eclipse, alongside calibration lamp spectra. The spatial location of strong emission lines and separation between lines were used to determine the pixel value of wavelengths and spectral range within each camera. Pixel locations for the expected wavelength of Fe ion emission lines were determined and later compared to coronal measurements made during the eclipse.

Instrumental line width broadening was calculated by measuring the width of the Gaussian fit, discussed in detail in Section 3.2, for spectral signatures of our calibration lamp sources at 534.1 nm for Ne I, 642.1 nm for Kr I, and 785.5 nm for Kr I. The calibration sources have narrow spectral line widths at known wavelengths, which were then adjusted to the wavelength of the Fe ion lines of interest via the formula:

$$\Delta\lambda_{\mathrm{Fe}} = \Delta\lambda_{\mathrm{cal}} * \frac{\lambda_{\mathrm{Fe}}}{\lambda_{\mathrm{cal}}}, \tag{2}$$

where $\Delta\lambda_{\mathrm{cal}}$ is the instrumental broadening measured from the calibration lamp source, λ_{Fe} is the wavelength of the Fe ion line of interest, and λ_{cal} is the wavelength of the calibration source. For all three channels, instrumental broadening of 0.044 to 0.046 nm was calculated.

A single spectral plot of flattened and corrected solar eclipse coronal data is displayed to illustrate that the wavelength sampling varied slightly between channels, with resolution

Figure 7 Spectra of calibration lamps compared to eclipse measurements. The *x*-axis indicates the detector pixels in the spectral (horizontal) direction, approximately halfway across the detector spatial (vertical) dimension. (a) Neon gas measurement plotted in black and an example eclipse measurement of Fe XIV in green. (b) Neon gas plotted in black and an eclipse measurement of Fe X in orange. (c) Krypton gas plotted in black and an eclipse measurement of Fe XI in red. In all cases, we have ensured that calibration emission lines do not saturate the cameras. and data from the brightest portion of the corona were chosen. Vertical units are arbitrary, with the coronal data scaled for visibility.
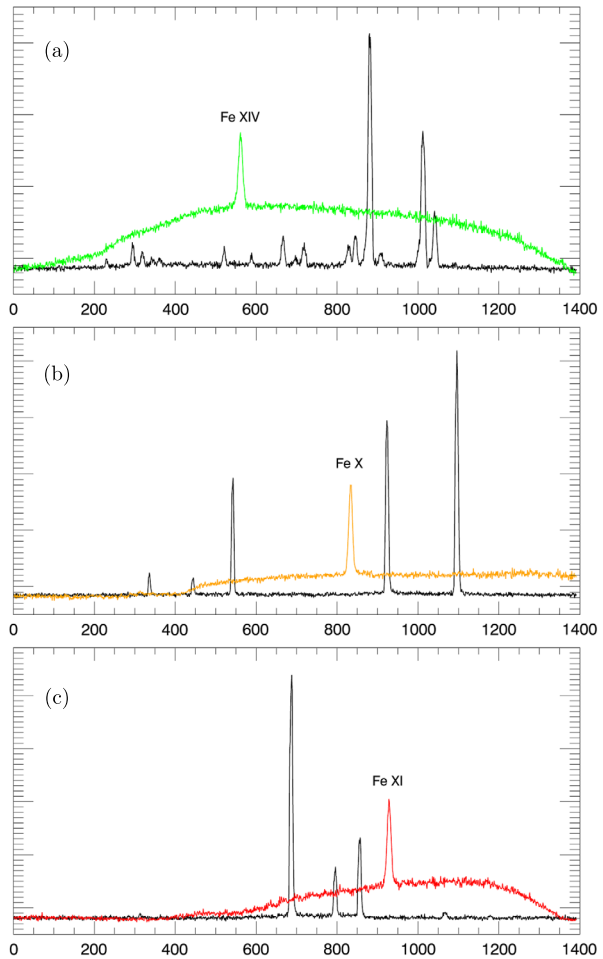
varying approximately 0.011 to 0.014 nm per pixel, and the full-width at half maximum (FWHM) of all the Fe lines less than 1 nm. The Fe ion emission lines spanned a range of 30, 30, and 40 pixels for Fe XIV, Fe X, and Fe XI, respectively.

3. Observational Analysis

This section describes the collection of data during totality, the analysis methods, and organization of results.

3.1. Data Collection

The total solar eclipse observations were made on 2019 July 2 at 20:40 UTC in Rodeo, Argentina ($-30.194°$, $-69.102°$), at an altitude of ≈ 1700 m. Conditions were clear, wind was minimal, and the Sun was elevated at $\approx 11.5°$ above the horizon. The device's internal temperature varied from 25.3 °C to 24.4 °C from the start to the end of totality.
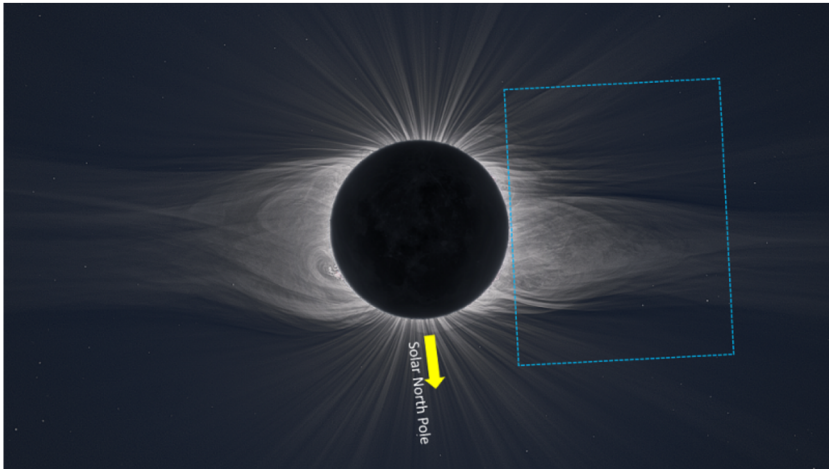
Figure 8 A high-resolution and processed composite of the corona in visible light as observed during the 2019 eclipse from Tres Cruses, Chile. The blue dotted rectangle displays the region of the corona selected for analysis. The spectrometer observed a larger region, but the restriction is made due to poor signal-to-noise ratio at larger distances from the Sun, and over the dim polar regions. Corresponding to the alignment of the instruments during this southern hemisphere eclipse, the Solar North Pole points approximately downward as indicated by the yellow arrow. The orientation of the image means that the left side of the Sun/corona is west, and rotates away from Earth, while the right side of the image is east and rotates towards the Earth. Image courtesy of Miloslav Druckmüller.

Light transmitted into the context camera displays a full image of the solar disk during the beginning of the eclipse in broadband visible white light, which allowed for locating the spectrometer entrance slit with respect to the solar limb. The context camera only covered $\approx 36' \times 47'$ of sky, an area far smaller than the spectrometer camera coverage, so white light imaging from this camera is used primarily for determining the initial pointing of the spectrometer during the first moments of totality.

Due to this limitation, spectrometer measurements are compared against large-scale white light structures in Figure 8, which were captured by Miloslav Druckmüller 150 km away in Tres Cruses, Chile, where the timing of the eclipse is approximately 1 minute prior to Rodeo, Argentina. This is considered a reliable contextual comparison since large-scale coronal structures tend not to change significantly within short timescales in the absence of CMEs. No large events were recorded during the few minutes of observation.

The spectrometer assembly tracked the Sun prior to totality, then tracking was turned off at the start of totality, thus the scanning of the corona by the spectrometer was entirely due to diurnal motion, whilst the spectrometer assembly was conveniently static. The motion of the spectrometer slit relative to the Sun during totality is shown in Figure 9, calculated by identifying the portion of the faint solar limb in the context camera images, and fitting circles using a method similar to that used for correcting the optical smile, as shown in Figure 6. The path of the Sun drifted slightly downwards in relation to the spectrometer slit during totality. A line was drawn through the center of the solar limb circles at the start and end of the eclipse. The line's endpoints were used to find that the solar path drifted 10.87° away from perfect horizontal motion, as illustrated in Figure 9, throughout the duration of totality. The solar path drift angle enabled us to map the time series of spectral data in relation to location in the corona.
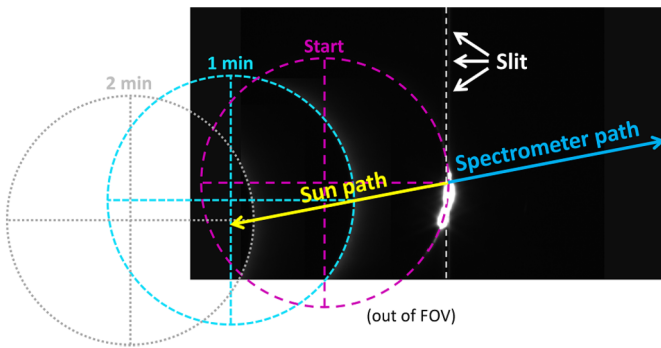
Figure 9 The visible outline of the solar limb is marked as dashed circles as it moves in relation to the spectrometer slit (white dashes) via diurnal motion. Once the path of the Sun is determined in yellow, the blue arrow notes the direction of the spectrometer with respect to the solar disk at the purple "Start" time. Purple, cyan, and grey circles display the Sun's position after 0, 1 and 2 minutes of totality, respectively. Note that for the start time, the context camera shows the location of the spectrometer slit as a faint grey vertical line.
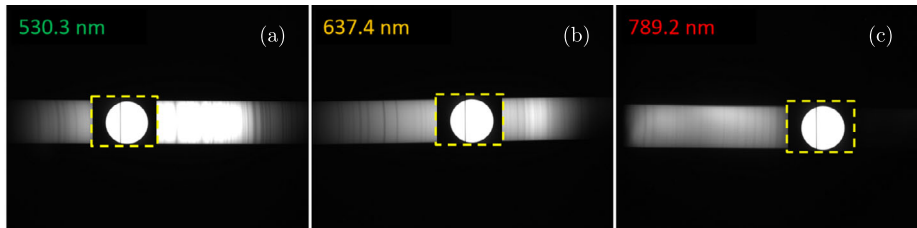

Figure 10 Context camera images, bounded by yellow dashed boxes, of the solar disk in (a) Fe XIV, (b) Fe X, and (c) Fe XI are overlain onto each channel's spectrometer measurements taken at the same time. The size of the yellow boxes is $\approx 35.2' \times 47.5'$ and the slit is situated on the solar disk, where each Fe emission line is located within the images. The vertical size of the spectrometer images is 156.3' and horizontal spectral range is (a) 15.0 nm, (b) 16.0 nm, and (c) 19.3 nm.

Figure 10 shows that the spectrometer slit sampled a much larger vertical portion of the sky than the context camera. After calibrations, misalignment factors appear to have had minimal effect on signal loss, since the brightest portion of the coronal spectra was well within the sensitive areas of the images.

Based on previous experience with signal response in the device, the Fe XIV, Fe X, and Fe XI spectrometer channels were set to capture a continuous series of exposures of 1, 1, and 4 seconds, respectively, throughout totality. Thus, the spectrometer panned across 0.25, 0.25, and 1 arcmin of sky during each exposure, with a 0.075 arcmin gap between each exposure due to data transfer overheads to give a total of 113, 114, and 34 spectral images captured in FITS format of 1392×1040 pixels. Totality lasted 134 seconds and 33.5 arcmin of apparent motion were recorded, although some data were discarded due to excess brightness during second and third contact.

3.2. Fitting Gaussian Functions to Emission Spectra

The coronal emission curves within Figure 7 show the result of flattened intensity reduction toward the center of the image frame, where relevant spectra are located, and emis-

Figure 11 Sample line profile of Fe XIV (points with red error bars) fitted with a Gaussian function (black line). The vertical axis of intensity is measured in DN and the horizontal axis is measured in pixels across the spectral image. The 1-σ error estimate for the intensity's fit is shown as red bars. The fitted Gaussian parameters are as follows: $A_0 = 1715.23 \pm 47.15$, $A_1 = 15.5 \pm 0.15$, $A_2 = 4.9 \pm 0.19$, $A_3 = 7450 \pm 45.87$, and $A_4 = -0.66 \pm 2.14$.
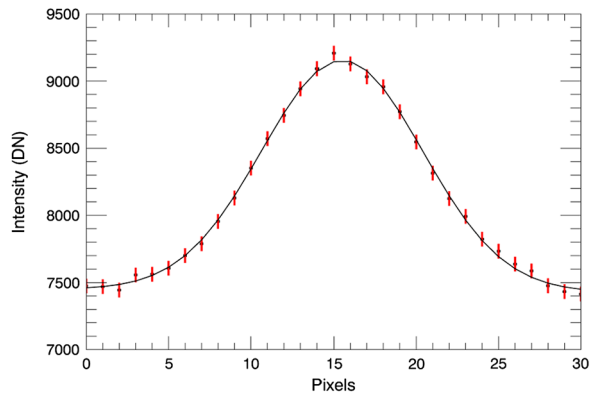
sion curves measured in a spectrometer from a single ion should appear as Gaussian-like shapes with intensity decreasing symmetrically away from the central peak wavelength. While highly dynamic events, such as flares and CMEs, can lead to skewed Gaussians, or more complicated shapes, the Sun was at solar minimum with very little activity. Thus, we utilized a non-linear least-squares fit with a Gaussian and a linear background:

$$f(x) = A_0 e^{\frac{-z^2}{2}} + A_3 + A_4 x, \tag{3}$$

where

$$z = \frac{x - A_1}{A_2}, \tag{4}$$

and x is the spectral pixel index, which following wavelength calibration can be replaced by the wavelength in nm. A_0 is the peak amplitude of the Gaussian, A_1 is the position of the Gaussian peak, A_2 is the Gaussian width (standard deviation), A_3 is the constant background term, and A_4 is the linear background term.

Prior to fitting, the data are convolved with a narrow, normalized 2D Gaussian kernel of 4 σ (standard deviation) in order to improve the signal-to-noise ratio, enable the fit in low-signal regions, and smooth the spectral image in both the horizontal spectral and vertical spatial directions. Following convolution, a spectral range of interest is extracted for each channel, of width 30, 30, and 40 pixels for each channel, respectively. These extracted spectra are then used for the Gaussian fitting. An example of a Gaussian fit to an eclipse measurement of Fe XIV is shown in Figure 11, where the points with red error bars show the measurement, and the black line the fitted Gaussian.

The Gaussian-fitting procedure is applied to each measured spectrum and the Gaussian parameters for each spatial pixel where a successful fit is achieved are recorded. Criteria for judging a fit as successful or not are based on thresholds on fitted parameters. For example, a value for the line width that is very narrow (e.g., 1 pixel or less) is obviously a non-valid fit, and is discarded. Such pixels are treated as missing data in our results. As expected, the fitting is generally more reliable near the solar limb, due to higher DN, where $22-25\%$ of the available 1040 pixels along the spectral slit are successfully fitted.
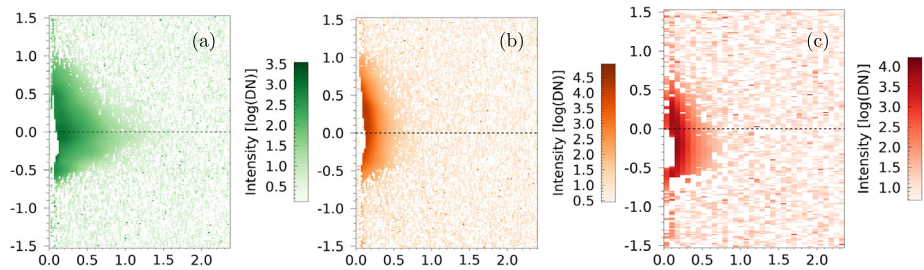
Figure 12 Maps of spectral line intensities for (a) Fe XIV, (b) Fe X, and (c) Fe XI. All units along the axes are solar radii, with the vertical axis originating at the solar center and the horizontal axis originating at the edge of the solar limb. We have used a color scheme representative of the green, reddish-orange, and near-infrared appearance of the emission lines. The horizontal dashed line in each panel shows the location of the height profiles of Figures 13, 14, and 15, respectively.

4. Results and Interpretation

4.1. Spectral Line Intensity Results

The results of the Gaussian fitting can be used to create a visual map of intensities (or other characteristics) as the spectrometer slit is scanned across the corona. Figure 12 shows that intensity is stronger near the equatorial-positioned dashed line, corresponding to the location of a large helmet streamer, as seen in white light in Figure 8. The Fe XIV ion measurements in Figure 12a, which corresponds to the hottest equilibrium temperature of 1.9 MK, extends furthest overall. The Fe X ion measurements in Figure 12b, and Fe XI ion measurements in Figure 12c coincide with cooler equilibrium temperatures of 0.9 and 1.3 MK, respectively, and are confined closer to the solar disk. Beyond $\approx 1\ R_\odot$ the measurements become noisy, there are a large number of pixels where the Gaussian fitting has failed, and the data can be considered largely unreliable.

In Figure 13a, the intensity of the spectral lines is compared for the first $\approx 1 R_\odot$ along the dashed horizontal line in Figure 12, where the signal is strongest and the Gaussian fits are most reliable. The fitting routine calculated the measurements error and are shown as shaded areas. Starting from the solar limb, the first intensity measurement with reliable Gaussian signal occurs at 0.15 $R_\odot$, where Fe X had the strongest initial DN and also weakened most rapidly with increasing distance. Both Fe X and XIV begin to show signal gaps between 10 to 20 DN, suggesting that instrumental noise was similar for both. Fe XI, the last ion measured within the spectrometer optical path, started with an intermediate DN and weakened less drastically than Fe X, disappearing around ≈ 40, likely due to higher instrumental noise. Fe X, in Figure 13c, and Fe XI, in Figure 13d, represent the two cooler ions and became less dominant at 0.3 $R_\odot$ while their signals became unreliable beyond 0.6 $R_\odot$. The hottest ion, Fe XIV in Figure 13b starts out with a much weaker intensity DN, yet it does not weaken as quickly with distance, and has the dominant DN from 0.3 to 1.0 $R_\odot$. It should be noted that error bars will appear visually larger on log graphs as measurements decrease.

Overall, these spectral intensity results can be interpreted in terms of the hydrostatic weighting bias of density scale heights for coronal loops. Aschwanden and Nitta (2000) showed that plasmas within flux tubes can be treated as isolated isothermal atmospheres, and their approximation showed that hotter flux tubes have larger density scale heights than cooler ones – thus this alone can account for the hotter channel maintaining intensity to greater distances.
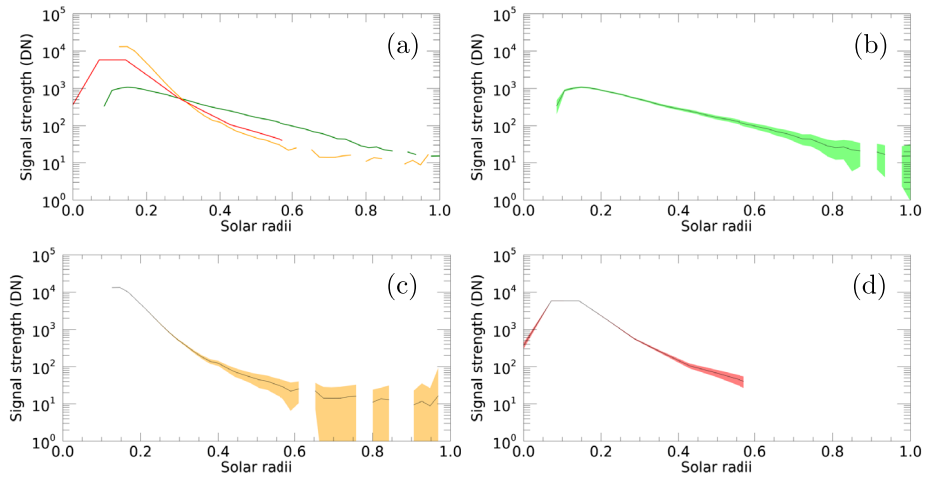
Figure 13 The intensity of Fe XIV in green, Fe X in orange and Fe XI in red as a function of distance along the horizontal dashed line of Figure 12. Gaps in data are due to a failure in fitting the line profiles with Gaussians, usually due to low DN. (a) A comparison of the line intensities in the highest DN regions within $\approx 1 \, R_\odot$ of the Sun. The other three plots show each line separately, (b) Fe XIV, (c) Fe X, and (d) Fe XI. The shaded regions show the estimated errors in intensity.
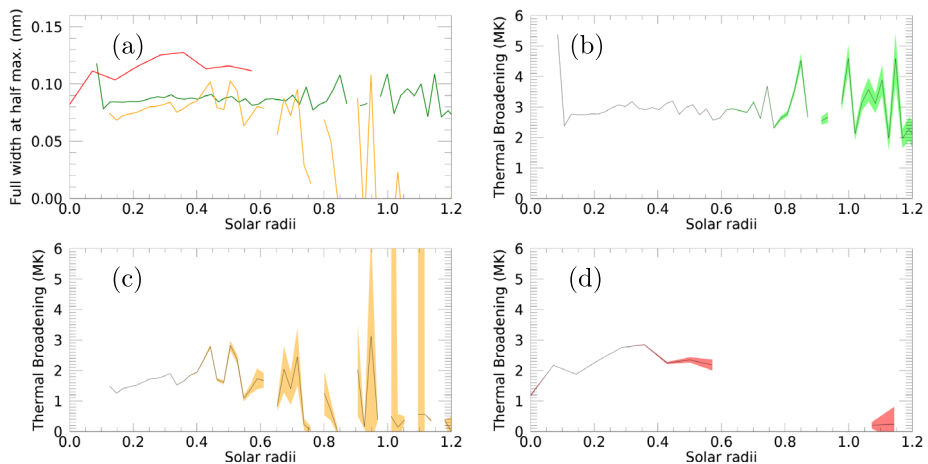

Figure 14 (a) The FWHM of Fe XIV in green, Fe X in orange, and Fe XI in red lines as a function of distance along the horizontal dashed line of Figure 12. Gaps in data are due to a failure in fitting the line profiles with Gaussians, usually due to low signal. The other panels show the direct conversion of the FWHM into a Doppler-broadening equivalent temperature of (b) Fe XIV, (c) Fe X, and (d) Fe XI. The shaded regions show the estimated errors.

4.2. Spectral Line Width Broadening

Figure 14a compares the FWHM of the spectral lines, converted from fitted Gaussian line widths, as a function of distance along the dashed horizontal line in Figure 12. Instrumental broadening, ≈ 0.045 nm for all channels, was first subtracted from these values and the fitting routine calculated the measurement errors that are shown as shaded areas. Within

the context of coronal emission spectra, the line width contains information on the thermal Doppler broadening, with further broadening caused by motions such as turbulence, bulk velocities, and wave motions (e.g. Mierla et al., 2008). From the solar limb to 0.6 $R_\odot$, the line width is similar for the Fe X and XIV lines, but considerably higher for the Fe XI line. FWHM is then converted to thermal broadening ion temperatures via:

$$T = \frac{m}{k_B 8 \ln 2} \left(\frac{c\lambda_F}{\lambda_0}\right)^2, \tag{5}$$

where m is the ion mass, k_B is the Boltzmann constant, c is the speed of light, λ_F is the FWHM, and λ_0 is the ion wavelength.

Our results show that the ion temperatures are at most 1.5 to 3 MK, as shown in the remaining plots in 14b, 14c, and 14d, for the first 0.6 $R_\odot$ above the solar limb. Beyond 0.6 $R_\odot$, there is a suggestion of a decrease in line width for the cooler Fe X ion relative to the hotter Fe XIV, although the DN becomes weak.

The thermal broadening temperatures measured are slightly over 1.5 times greater than the equilibrium temperature associated with each of the Fe ions. Cranmer, Panasyuk, and Kohl (2008) showed that strong temperature anisotropies for heavy ions are due to preferential ion heating and acceleration at elevations just above our data. In particular, their UVCS measurements of temperature perpendicular to the magnetic field were much larger than the temperature parallel to the field. Considering the off-limb orientation of Fe XIV, as suggested by Doppler velocity measurements in Figure 15b, to be nearly tangential to our LOS, it is likely that true temperature anisotropy is the reason for enhanced thermal broadening. The temperature anisotropy is achieved via the mechanism described in Lu and Li (2007), where ions are picked up in the transverse direction by the Alfvén wave, obtain an average transverse velocity, then parallel thermal nonresonant motions produce phase randomizations between ions and this interaction leads to ion heating.

Unresolved motions, or non-thermal broadening, are thought to be associated with turbulence or quasi-periodic upflows and a helmet streamer that extends off-limb will consist mostly of interconnected magnetic fields that are perpendicular to the spectrometer LOS. In this case, small-scale twists and Alfvén waves are likely to play a role in non-thermal line broadening (Aschwanden, 2019). Turbulent motion differences could also be attributed to this separation in line width broadening, as energy converts from Alfvén waves to acoustic waves in a near-collisionless part of the corona. Resolving the non-thermal component of line width broadening relies heavily on knowing the plasma temperature in detail and our cross-calibration technique in Section 2.3 was performed on an integrating sphere, so using a line ratio technique to estimate the coronal temperature would come with many compromises as compared to coronal calibrations, which were not possible due to the short period of totality. Lacking a secondary measure for reliable plasma temperature, we have assumed that FWHM line width measurements are due to "thermal" broadening, but non-thermal broadening in the low corona is likely to be a key contributor due to the complex magnetic structure where plasma flow is chaotic. Although, the overall line width trend, within our measured heights, is that low signal leads to significant line width variation at increasing heights and may not be representative of the whole corona at these heights. Although, the quasi-decrease in Fe X and XI line widths may suggest that kinetic temperature may instead be the primary driver for the decrease with distance (Mierla et al., 2008).

4.3. LOS Doppler Velocities

Figure 15a displays the fitted center of the spectral line as a function of spectral distance, and gives the bulk ion velocity in km s^{-1} for Fe XIV in Figure 15b, Fe X in Figure 15c, and
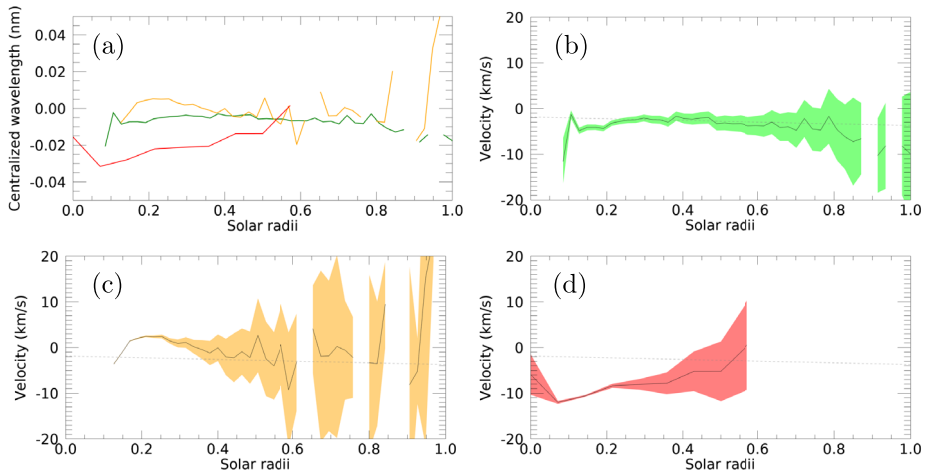
Figure 15 (a) Doppler shift of the Fe XIV in green, Fe X in orange, and Fe XI in red lines as a function of distance along the horizontal dashed line of Figure 12. Gaps in data are due to a failure in fitting the line profiles with Gaussians, usually due to low signal. The expected stationary wavelength of each Fe ion is represented at 0 nm. The other panels show the conversion of the Doppler shift into a LOS Doppler velocity for (b) Fe XIV, (c) Fe X, and (d) Fe XI. The shaded regions show the estimated errors. The grey dashed line represents the velocity expected for solid body rotational velocity based upon the Carrington rotation (thus increasingly negative with increasing distance from the disk).

Fe XI in Figure 15d along the LOS via the Doppler shift formula:

$$V = \frac{\lambda_D}{\lambda_0} c, \tag{6}$$

where λ_D is the centralized wavelength. The fitting routine calculated the measurements error and are shown as shaded areas. Such bulk motions in the coronal context should include a component due to solar rotation. Our measurements were made on the side of the corona rotating toward the Earth, suggesting $-1.9 \ \mathrm{km\,s^{-1}}$ due to blueshift at the photosphere if the solar atmosphere was treated as a rigid, rotating "solid" magnetic body that speeds up with increasing $R_\odot$ in the corona. This solid body rotation rate is visualized as baselines of grey dashed lines in Figure 15b-d. The Doppler shifts of the hotter Fe XIV line is fairly consistent with the expected coronal rotation beyond 0.25 $R_\odot$. In contrast, the cooler lines show large variations below $\approx 0.5 \ R_\odot$, and are quite different from each other. Below 0.4 $R_\odot$, Fe XI has a notable increase in velocity, at roughly eight times what would be expected of a radial corona rotating with the photosphere. A peak (negative) speed of $-12 \ \mathrm{km\,s^{-1}}$ is measured at 0.07 $R_\odot$. The coolest Fe X ion moves rapidly in the opposite direction of rotation, peaking at $+2.5 \ \mathrm{km\,s^{-1}}$ (redshift) below $\approx 0.2 \ R_\odot$ and then transitions to blueshifts above 0.3 $R_\odot$. Above 0.7 $R_\odot$, both Fe X and Fe XI show large variations that are likely due to poor line fitting.

We interpret these mixed results in the context of the complex large-scale magnetic structure of helmet streamers in the low corona, superimposed on the general coronal solid-body rotation displayed in Figure 15b. Below $\approx 0.5 \ R_\odot$, we expect the helmet streamer to be composed of a system of large, nested magnetic loops. Qualitatively, this can be seen in the processed white-light image of Figure 8. These loops, whilst generally aligned in a north–south orientation, may also have a longitudinal component, and bulk motion of ions along

these loop systems may lead to the measured Doppler shifts. Large-scale systems of loops aligned at different orientations to the LOS may have different temperatures, and can lead to the different profiles of Doppler shifts seen in the three ion lines. We note also that the corona does not rotate rigidly with the photosphere, and can possess rotation rates that vary by several degrees per day depending on latitude, and solar cycle phase (Morgan, 2011; Edwards et al., 2022). According to Edwards et al. (2022), the equatorial coronal rotation rate at a distance of 4 $R_\odot$ during the time of the eclipse is generally slightly slower than the Carrington rotation rate, but the effect is small.

5. Summary

Overall, the end of Solar Cycle 24 was a below-average solar minimum, with very little activity. This period exhibited few flares, CMEs, and coronal brightness was low in general. On 2019 July 2, there was a large helmet streamer in the east, shown in Figure 8, which is the subject of our study. We note that no large CMEs were reported during the period of the total eclipse.

Our results show several interesting features of the helmet streamer, including (i) different rates of intensity decrease with increasing distance between the cooler and hotter lines, (ii) different line widths between the cooler and hotter lines, and (iii) different profiles of Doppler shift between all channels.

The first feature can be easily explained. LOS observations within helmet streamers will always contain a variety of flux tubes at different isothermal temperatures. Assuming hydrostatic equilibrium, the observed density stratification of cooler flux tubes will be biased towards the solar limb, thus hotter flux tubes will dominate in observations at larger distances above the solar limb. The second feature is consistent with a mechanism that enables the heating of ions by low-frequency, parallel-propagating Alfvén waves in a low-β plasma. The heating mechanism operates via parallel thermal motions producing phase randomizations, which leads to heating dominant in the direction perpendicular to the background magnetic field and produces a large ion temperature anisotropy. The third feature can be interpreted in terms of large-scale systems of closed loops forming the base of the helmet streamer, with bulk plasma motions along the loop systems, and regions of different temperatures dominating the signal from different channels.

This interpretation is consistent with our spectrometer measurements as the coolest ion, Fe X, dominates at low distances and weakens in DN most rapidly with increasing height. Additionally, the warmest ion, Fe XIV, maintains a more evenly distributed DN overall and becomes dominant at larger distances above the solar limb. Consistent thermal broadening of Fe XIV in Figure 14b also supports the interpretation of an isothermal flux tube with a consistent temperature and density structure extending farther than the other Fe ions.

The three spectral lines show strong deviations in Doppler velocity within the first 0.4 $R_\odot$ above the limb for Fe X and XI. For Fe X, the LOS velocity near 0.2 to 0.3 $R_\odot$ shows motion in the opposite direction of overall rotation and could be understood as a large loop structure extending from the photosphere on the side facing the Earth, with plasma flowing temporarily down the loop. Similarly, for Fe XI, the LOS velocity near 0.1 to 0.4 $R_\odot$ moves much faster than overall rotation. This could be interpreted as the same type of loop structure with descending plasma on the far side beyond the solar limb. The size of such loop structures could be similar in size to those within the helmet streamer, but from an Earth observer's point of view, they would not extend as far in distance above the solar disk. This hypothetical orientation of magnetic loops is consistent with the DN of Fe X and XI decreasing more rapidly than Fe XIV, as shown in Figure 13.
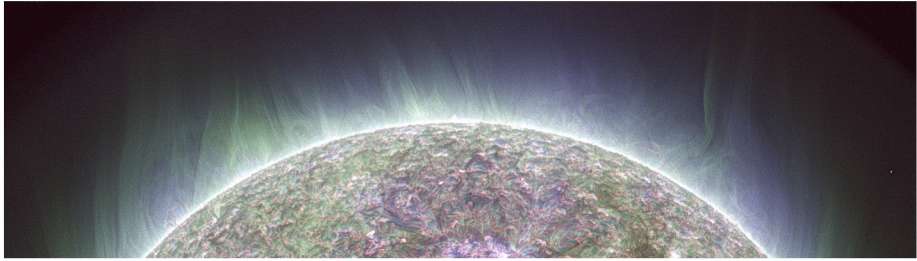
Figure 16 A rotated, context image from SDO/AIA on 2019 July 2 at 20:40 UT. The spectrometer observation began midway and scanned towards the top. All seven SDO/AIA channels contribute to this composite, with the temperature response of each channel between 0.05 and 7.0 MK specifying that channel's contribution to the red, green, and blue color channels of the output images. The image is processed with Multi-scale Gaussian Normalization to enhance fine-scale structure (Morgan and Druckmüller, 2014).

The interconnectedness of magnetic loops, shown in Figures 8 and 16 in spatially enhanced visible and ultraviolet imagery, respectively, makes it difficult to distinguish individual field lines or coronal loops at either the base level or above the solar limb. Upon close inspection, the field lines extending above the solar limb cross each other and intersect all of the faint coronal loops from Earth's point of view. This intertwined loop structure implies that ionization is a result of reconnection or 'snapping' of magnetic fieldlines and thus induces ionization, rather than the kinetic temperature alone. This may also account for the prevalence of the hottest ion, Fe XIV, in the low corona as the overall most common Fe ion during our observation, as the interconnected structure of coronal loops within helmet streamers are likely to release energy via reconnection.

The strong overall nature of magnetism in helmet streamers leads to the possibility that the coronal rotation is decoupled from the photosphere and more likely is tied to rotation rates deeper within the convection zone. Since our coronal measurements suggest super rotation with respect to the photosphere, this result is consistent with Poynting-Robertson-like photon induced drag as described by Kuhn et al. (2012). In this model, the core and radiation zone are treated as a mechanically 'solid' radiating body without fluid motion, so as photons scatter within the plasma there is no net change in angular momentum overall. As photons diffuse outwards to the fluid-like convective zone, they interact with moving plasma and result in a net loss of the plasma's angular momentum as they radiate away at the surface. This effect produces a mild braking force within the plasma that is most efficient at the outer edge of the Sun, while deeper layers that govern the magnetic fields which extend out to the corona are not slowed down.

Normally, the brightness of the solar disk drastically overwhelms attempts at ground-based observation of the solar atmosphere due to scattered light. This makes observing the lower corona in visible wavelengths a challenge. In the absence of a coronagraph instrument, it is only during the brief moments of a total solar eclipse that there is an opportunity to directly measure visible light spectra of the corona without contamination from the solar disk. In this study, a high-resolution spectrometer was built to measure the spectral lines of Fe X, XI, and XIV ions. The equilibrium temperatures of these ions, ranging from 0.9 to 1.9 MK, are thought to be representative of overall coronal temperatures. This study is a proof-of-concept, and shows how a relatively low-cost instrument, used during an eclipse, can provide valuable diagnostics. Coupled with a coronagraph system on a space mission, such an instrument can provide routine measurements that would greatly increase our understanding of the complex low corona. Such an instrument would have the benefit of increased

exposure duration, enabling far higher signal-to-noise, and diagnostics to distances considerably beyond those gathered during the eclipse. Measurements of intensity, line widths, and Doppler shifts, compared between the three visible lines from the same ion, and available over extended periods of time, can give insights into the structure and dynamics of the lower corona, and, in particular, the nascent slow solar wind in helmet streamers.

Author contributions Gabriel D. Muro was in charge of the direction of the project, performed the field observation, collected data, set up the equipment, conceived and performed all calibrations, conceived and performed all data analysis, wrote all necessary code, wrote all sections of the manuscript. Matt Gunn fabricated the spectrometer, provided instruments necessary for calibration, gave valuable feedback on the operation of the spectrometer. Stephen Fearn acted as field technician, assisted in the field observation, and assisted in set up of equipment. Tomos Fearn set up the field computer, set up camera software, and wrote code that synchronized image timings. Huw Morgan conceived of the original idea, secured funding for the project, gave major feedback in the writing of the manuscript, assisted in writing of all data analysis code, verified the analytic methods, and supervised the project overall

Data Availability The datasets generated during and/or analyzed during the current study are available from the corresponding author on reasonable request. The AIA/SDO data used here were obtained through the cutout service of the Virtual Observatory package of Solar Software, and is courtesy of NASA/SDO and the AIA science team. The processed composite of the corona is available at Miloslav Druckmuller's website: http://www.zam.fme.vutbr.cz/~druck/eclipse/.

Declarations

Competing interests The authors declare no competing interests.

References

Alzate, N., Habbal, S.R., Druckmüller, M., Emmanouilidis, C., Morgan, H.: 2017, Dynamics of large-scale coronal structures as imaged during the 2012 and 2013 total solar eclipses. *Astrophys. J.* **848**, 84. DOI.

Alzate, N., Morgan, H., Viall, N., Vourlidas, A.: 2021, Connecting the low to the high corona: a method to isolate transients in STEREO/COR1 images. *Astrophys. J.* **919**, 98. DOI.

SPICE Consortium, Anderson, M., Appourchaux, T., Auchère, F., Aznar Cuadrado, R., Barbay, J., Baudin, F., Beardsley, S., Bocchialini, K., Borgo, B., Bruzzi, D., Buchlin, E., Burton, G., Büchel, V., Caldwell, M., Caminade, S., Carlsson, M., Curdt, W., Davenne, J., Davila, J., DeForest, C.E., Del Zanna, G., Drummond, D., Dubau, J., Dumesnil, C., Dunn, G., Eccleston, P., Fludra, A., Fredvik, T., Gabriel, A., Giunta, A., Gottwald, A., Griffin, D., Grundy, T., Guest, S., Gyo, M., Haberreiter, M., Hansteen, V., Harrison, R., Hassler, D.M., Haugan, S.V.H., Howe, C., Janvier, M., Klein, R., Koller, S., Kucera,

T.A., Kouliche, D., Marsch, E., Marshall, A., Marshall, G., Matthews, S.A., McQuirk, C., Meining, S., Mercier, C., Morris, N., Morse, T., Munro, G., Parenti, S., Pastor-Santos, C., Peter, H., Pfiffner, D., Phelan, P., Philippon, A., Richards, A., Rogers, K., Sawyer, C., Schlatter, P., Schmutz, W., Schühle, U., Shaughnessy, B., Sidher, S., Solanki, S.K., Speight, R., Spescha, M., Szwec, N., Tamiatto, C., Teriaca, L., Thompson, W., Tosh, I., Tustain, S., Vial, J.-C., Walls, B., Waltham, N., Wimmer-Schweingruber, R., Woodward, S., Young, P., De Groof, A., Pacros, A., Williams, D., Müller, D.: 2020, The Solar Orbiter SPICE instrument – an extreme UV imaging spectrometer. *Astron. Astrophys.* **642**, A14. DOI.

Antonucci, E.: 2000, Fast solar wind velocity in a polar coronal hole during solar minimum. *Solar Phys.* **197**, 115. DOI.

Aschwanden, M.J.: 2019, *New Millennium Solar Physics*, Springer, Berlin. DOI.

Aschwanden, M.J., Nitta, N.: 2000, The effect of hydrostatic weighting on the vertical temperature structure of the solar corona. *Astrophys. J.* **535**, L59. DOI.

Beckman, J., Begot, J., Charvin, P., Hall, D., Lena, P., Soufflot, A., Liebenberg, D., Wraight, P.: 1973, Eclipse flight of Concorde 001. *Nature* **246**, 72. DOI.

Boe, B., Habbal, S., Druckmüller, M., Landi, E., Kourkchi, E., Ding, A., Starha, P., Hutton, J.: 2018, The first empirical determination of the Fe10+ and Fe13+ freeze-in distances in the solar corona. *Astrophys. J.* **859**, 155. DOI.

Cranmer, S.R., Gibson, S.E., Riley, P.: 2017, Origins of the ambient solar wind: implications for space weather. *Space Sci. Rev.* **212**, 1345. DOI.

Cranmer, S.R., Panasyuk, A.V., Kohl, J.L.: 2008, Improved constraints on the preferential heating and acceleration of oxygen ions in the extended solar corona. *Astrophys. J.* **678**, 1480. DOI.

Cranmer, S.R., Kohl, J.L., Noci, G., Antonucci, E., Tondello, G., Huber, M.C.E., Strachan, L., Panasyuk, A.V., Gardner, L.D., Romoli, M., Fineschi, S., Dobrzycka, D., Raymond, J.C., Nicolosi, P., Siegmund, O.H.W., Spadaro, D., Benna, C., Ciaravella, A., Giordano, S., Habbal, S.R., Karovska, M., Li, X., Martin, R., Michels, J.G., Modigliani, A., Naletto, G., O'Neal, R.H., Pernechele, C., Poletto, G., Smith, P.L., Suleiman, R.M.: 1999, An empirical model of a polar coronal hole at solar minimum. *Astrophys. J.* **511**, 481. DOI.

Culhane, J.L., Harra, L.K., James, A.M., Al-Janabi, K., Bradley, L.J., Chaudry, R.A., Rees, K., Tandy, J.A., Thomas, P., Whillock, M.C.R., Winter, B., Doschek, G.A., Korendyke, C.M., Brown, C.M., Myers, S., Mariska, J., Seely, J., Lang, J., Kent, B.J., Shaughnessy, B.M., Young, P.R., Simnett, G.M., Castelli, C.M., Mahmoud, S., Mapson-Menard, H., Probyn, B.J., Thomas, R.J., Davila, J., Dere, K., Windt, D., Shea, J., Hagood, R., Moye, R., Hara, H., Watanabe, T., Matsuzaki, K., Kosugi, T., Hansteen, V., Wikstol, Ø.: 2007, The EUV imaging spectrometer for hinode. *Solar Phys.* **243**, 19. DOI.

Del Zanna, G., Samra, J., Monaghan, A., Madsen, C., Bryans, P., DeLuca, E., Mason, H., Berkey, B., de Wijn, A., Rivera, Y.J.: 2023, Coronal densities, temperatures, and abundances during the 2019 total solar eclipse: the role of multiwavelength observations in coronal plasma characterization. *Astrophys. J. Suppl.* **265**, 11. DOI.

Ding, A., Habbal, S.R.: 2017, First detection of prominence material embedded within a 2×10^6 K CME front streaming away at 100–1500 km s^{-1} in the solar corona. *Astrophys. J.* **842**, L7. DOI.

Domingo, V., Fleck, B., Poland, A.I.: 1995, The SOHO mission: an overview. *Solar Phys.* **162**, 1. DOI.

Druckmüller, M., Rušin, V., Minarovjech, M.: 2006, A new numerical method of total solar eclipse photography processing. *Contrib. Astron. Obs. Skaln. Pleso* **36**, 131. ADS.

Edlén, B.: 1941, *An Attempt to Identify the Emission Lines in the Spectrum of the Solar Corona* **28**, Kungliga Svenska Vetenskapsakademien.

Edwards, L., Kuridze, D., Williams, T., Morgan, H.: 2022, A solar-cycle study of coronal rotation: large variations, rapid changes, and implications for solar-wind models. *Astrophys. J.* **928**, 42. DOI.

Gabriel, A.H., Garton, W.R.S., Goldberg, L., Jones, T.J.L., Jordan, C., Morgan, F.J., Nicholls, R.W., Parkinson, W.J., Paxton, H.J.B., Reeves, E.M., Shenton, C.B., Speer, R.J., Wilson, R.: 1971, Rocket observations of the ultraviolet solar spectrum during the total eclipse of 1970 March 7. *Astrophys. J.* **169**, 595. DOI. ADS.

Guhathakurta, M., Rottman, G.J., Fisher, R.R., Orrall, F.Q., Altrock, R.C.: 1992, Coronal density and temperature structure from coordinated observations associated with the total solar eclipse of 1988 March 18. *Astrophys. J.* **388**, 633. DOI. ADS.

Habbal, S.R., Esser, R., Arndt, M.B.: 1993, How reliable are coronal hole temperatures deduced from observations? *Astrophys. J.* **413**, 435. DOI. ADS.

Habbal, S.R., Morgan, H., Druckmüller, M.: 2014, Exploring the prominence-corona connection and its expansion into the outer corona using total solar eclipse observations. *Astrophys. J.* **793**, 119. DOI.

Habbal, S.R., Woo, R., Fineschi, S., O'Neal, R., Kohl, J., Noci, G., Korendyke, C.: 1997, Origins of the slow and the ubiquitous fast solar wind. *Astrophys. J.* **489**, L103. DOI.

Habbal, S.R., Morgan, H., Johnson, J., Arndt, M.B., Daw, A., Jaeggli, S., Kuhn, J., Mickey, D.: 2007a, Erratum: "Localized enhancements of Fe+10 density in the corona as observed in Fe XI 789.2 nm during the 2006 March 29 total solar eclipse" (ApJ, 663, 598 [2007]). *Astrophys. J.* **670**, 1521. DOI.

Habbal, S.R., Morgan, H., Johnson, J., Arndt, M.B., Daw, A., Jaeggli, S., Kuhn, J., Mickey, D.: 2007b, Localized enhancements of Fe+10 density in the corona as observed in Fe XI 789.2 nm during the 2006 March 29 total solar eclipse. *Astrophys. J.* **663**, 598. DOI.

Habbal, S.R., Druckmüller, M., Morgan, H., Daw, A., Johnson, J., Ding, A., Arndt, M., Esser, R., Rušin, V., Scholl, I.: 2009, Mapping the distribution of electron temperature and Fe charge states in the corona with total solar eclipse observations. *Astrophys. J.* **708**, 1650. DOI.

Habbal, S.R., Druckmüller, M., Morgan, H., Scholl, I., Rušin, V., Daw, A., Johnson, J., Arndt, M.: 2010, Total solar eclipse observations of hot prominence shrouds. *Astrophys. J.* **719**, 1362. DOI.

Ichimoto, K., Kumagai, K., Sano, I., Kobiki, T., Sakurai, T., Muñoz, A.: 1996, Measurement of the coronal electron temperature at the total solar eclipse on 1994 November 3. *Publ. Astron. Soc. Japan* **48**, 545. DOI.

Jarrett, A.H., von Klüber, H.: 1955, Interferometric measurements of the green corona line during the total solar eclipse of 1954 June 30. *Mon. Not. Roy. Astron. Soc.* **115**, 343. DOI.

Jarrett, A.H., von Klüber, H.: 1961, Interferometric investigation of emission lines of the solar corona during the total solar eclipse of 1958 October 12. *Mon. Not. Roy. Astron. Soc.* **122**, 223. DOI.

Kaufman, V.: 1993, Wavelengths and energy levels of neutral Kr-84 and level shifts in all Kr even isotopes. *J. Res. Natl. Inst. Stand. Technol.* **98**, 717. DOI.

Kohl, J.L., Esser, R., Gardner, L.D., Habbal, S., Daigneau, P.S., Dennis, E.F., Nystrom, G.U., Panasyuk, A., Raymond, J.C., Smith, P.L., Strachan, L., Ballegooijen, A.A.V., Noci, G., Fineschi, S., Romoli, M., Ciaravella, A., Modigliani, A., Huber, M.C.E., Antonucci, E., Benna, C., Giordano, S., Tondello, G., Nicolosi, P., Naletto, G., Pernechele, C., Spadaro, D., Poletto, G., Livi, S., Lühe, O.V.D., Geiss, J., Timothy, J.G., Gloeckler, G., Allegra, A., Basile, G., Brusa, R., Wood, B., Siegmund, O.H.W., Fowler, W., Fisher, R., Jhabvala, M.: 1995, The ultraviolet coronagraph spectrometer for the Solar and Heliospheric Observatory. *Solar Phys.* **162**, 313. DOI.

Kohl, J.L., Noci, G., Cranmer, S.R., Raymond, J.C.: 2006, Ultraviolet spectroscopy of the extended solar corona. *Astron. Astrophys. Rev.* **13**, 31. DOI.

Koutchmy, S., Belmahdi, M., Coulter, R.L., Demoulin, P., Gaizauskas, V., MacQueen, R.M., Monnet, G., Mouette, J., Noens, J.C., November, L.J.: 1994, CFHT eclipse observation of the very fine-scale solar corona. *Astron. Astrophys.* **281**, 249. ADS.

Kuhn, J.R., Bush, R., Emilio, M., Scholl, I.F.: 2012, The precise solar shape and its variability. *Science* **337**, 1638. DOI.

Léna, P., Viala, Y., Hall, D., Soufflot, A.: 1974, The thermal emission of the dust corona during the eclipse of June 30, 1973. II. Photometric and spectral observations. *Astron. Astrophys.* **37**, 81. ADS.

Li, X., Habbal, S.R., Kohl, J.L., Noci, G.: 1998, The effect of temperature anisotropy on observations of Doppler dimming and pumping in the inner corona. *Astrophys. J.* **501**, L133. DOI.

Lu, Q., Li, X.: 2007, Heating of ions by low-frequency Alfven waves. *Phys. Plasmas* **14**, 042303. DOI.

McComas, D.J., Christian, E.R., Cohen, C.M.S., Cummings, A.C., Davis, A.J., Desai, M.I., Giacalone, J., Hill, M.E., Joyce, C.J., Krimigis, S.M., Labrador, A.W., Leske, R.A., Malandraki, O., Matthaeus, W.H., McNutt, R.L., Mewaldt, R.A., Mitchell, D.G., Posner, A., Rankin, J.S., Roelof, E.C., Schwadron, N.A., Stone, E.C., Szalay, J.R., Wiedenbeck, M.E., Bale, S.D., Kasper, J.C., Case, A.W., Korreck, K.E., MacDowall, R.J., Pulupa, M., Stevens, M.L., Rouillard, A.P.: 2019, Probing the energetic particle environment near the Sun. *Nature* **576**, 223. DOI.

Menzel, D.H.: 1930, A study of the solar chromosphere based upon photographs of the flash spectrum taken by Dr. William Wallace Campbell, Director of the Lick Observatory, at the total eclipses of the Sun in 1898, 1900, 1905 and 1908. *Publ. Lick Obs.* **17**, 1. ADS.

Menzel, D.H., Pasachoff, J.M.: 1968, On the obliteration of strong Fraunhofer lines by electron scattering in the solar corona. *Publ. Astron. Soc. Pac.* **80**, 458. DOI.

Mierla, M., Schwenn, R., Teriaca, L., Stenborg, G., Podlipnik, B.: 2008, Analysis of the Fe X Fe XIVe width in the solar corona using LASCO-C1 spectral data. *Astron. Astrophys.* **480**, 509. DOI.

Morgan, H.: 2011, The rotation of the white light solar corona at height 4 $R_\odot$ from 1996 to 2010: a tomographical study of large angle and spectrometric coronagraph C2 observations. *Astrophys. J.* **738**, 189. DOI.

Morgan, H.: 2021, Daily variations of plasma density in the solar streamer belt. *Astrophys. J.* **922**, 165. DOI.

Morgan, H., Cook, A.C.: 2020, The width, density, and outflow of solar coronal streamers. *Astrophys. J.* **893**, 57. DOI.

Morgan, H., Druckmüller, M.: 2014, Multi-scale Gaussian normalization for solar image processing. *Solar Phys.* **289**, 2945. DOI.

Morgan, H., Habbal, S.R.: 2005, The impact of sunspots on the interpretation of coronal observations of the O VI doublet. *Astrophys. J.* **630**, L189. DOI.

Morgan, H., Habbal, S.R.: 2010, Observational aspects of the three-dimensional coronal structure over a solar activity cycle. *Astrophys. J.* **710**, 1. DOI.

Morgan, H., Habbal, S.R., Li, X.: 2004, Hydrogen Lyα intensity oscillations observed by the solar and helio-spheric observatory ultraviolet coronagraph spectrometer. *Astrophys. J.* **605**, 521. DOI.

Parker, E.N.: 1988, Nanoflares and the solar X-ray corona. *Astrophys. J.* **330**, 474. DOI. ADS.

Quémerais, E., Lamy, P.: 2002, Two-dimensional electron density in the solar corona from inversion of white light images – application to SOHO/LASCO-C2 observations. *Astron. Astrophys.* **393**, 295. DOI.

Reginald, N.L., Cyr, O.C.S., Davila, J.M., Brosius, J.W.: 2003, Electron temperature and speed measurements in the low solar corona: results from the 2001 June eclipse. *Astrophys. J.* **599**, 596. DOI.

Saloman, E.B., Sansonetti, C.J.: 2004, Wavelengths, energy level classifications, and energy levels for the spectrum of neutral neon. *J. Phys. Chem. Ref. Data* **33**, 1113. DOI.

Samra, J.E., Madsen, C.A., Cheimets, P., DeLuca, E.E., Golub, L., Marquez, V., Reyes, N.T.: 2022, New observations of the IR emission corona from the 2019 July 2 eclipse flight of the airborne infrared spectrometer. *Astrophys. J.* **933**, 82. DOI.

Singh, J., Bappu, M.K.V., Saxena, A.K.: 1982, Eclipse observations of coronal emission lines. I. [Fex] 6374Å profiles at the eclipse of 16 February 1980. *J. Astrophys. Astron.* **3**, 249. DOI.

Suleiman, R.M., Kohl, J.L., Panasyuk, A.V., Ciaravella, A., Cranmer, S.R., Gardner, L.D., Frazin, R., Hauck, R., Smith, P.L., Noci, G.: 1999, *Space Sci. Rev.* **87**, 327. DOI.

Tsurutani, B.T., Gonzalez, W.D., Gonzalez, A.L.C., Guarnieri, F.L., Gopalswamy, N., Grande, M., Kamide, Y., Kasahara, Y., Lu, G., Mann, I., McPherron, R., Soraas, F., Vasyliunas, V.: 2006, Corotating solar wind streams and recurrent geomagnetic activity: a review. *J. Geophys. Res. Space Phys.* **111**, A07S01. DOI.

Tu, C.-Y., Zhou, C., Marsch, E., Xia, L.-D., Zhao, L., Wang, J.-X., Wilhelm, K.: 2005, Solar wind origin in coronal funnels. *Science* **308**, 519. DOI.

Van Doorsselaere, T., Srivastava, A.K., Antolin, P., Magyar, N., Vasheghani Farahani, S., Tian, H., Kolotkov, D., Ofman, L., Guo, M., Arregui, I., et al.: 2020, Coronal heating by MHD waves. *Space Sci. Rev.* **216**, 140. DOI.

Yuan, L., Xie, J., He, Z., Wang, Y., Wang, J.: 2019, Optical design and evaluation of airborne prism-grating imaging spectrometer. *Opt. Express* **27**, 17686. DOI.